Nanoscale Advances

ROYAL SOCIETY OF CHEMISTRY

PAPER

View Article Online
View Journal | View Issue

Open Access Article. Published on 28 July 2025. Downloaded on 11/2/2025 4:17:36 AM.
This article is licensed under a Creative Commons Attribution-NonCommercial 3.0 Unported Licence.

Check for updates

Cite this: *Nanoscale Adv.*, 2025, **7**, 5720

A compartment-free digital plasmonic coupling assay *via* single-particle imaging and counting

Shengwei Zhang, Sina Jamalzadegan, Yan Wang,† Natalie Kelmer and Qingshan Wei *

Received 25th April 2025
Accepted 25th July 2025

DOI: 10.1039/d5na00403a

rsc.li/nanoscale-advances

Plasmonic coupling-based biosensors have been conventionally quantified by bulk spectroscopic or color measurement methods. Such detection schemes limit assay sensitivity due to the high background noise of bulk measurement. In this work, we developed a digital plasmonic assay platform for sensitive biomarker detection by enumerating individual plasmon-shifted nanoclusters *via* single-nanoparticle darkfield scattering imaging. The assay is based on a pair of gold (Au) and silver (Ag) nanoparticles (NPs) that are functionalized with high-affinity surface ligands such as antibodies for target recognition. Molecular binding induces the formation of nanoparticle clusters with plasmonic features distinct from those of individual Au or Ag NPs, which can be counted digitally without the need for complex chip or droplet compartments. We systematically investigated nanoparticle–protein interactions during bioconjugation and revealed different effects of absorbed proteins on nanoparticle stability. Under optimized conditions, we achieved a limit of detection (LOD) of 107.5 fM for the detection of biotinylated gold nanoparticles with this assay. FDTD simulation was also performed to investigate different plasmonic coupling effects of various Au–Ag, Ag–Ag, and Au–Au combinations. Finally, a particle counting algorithm was developed to quantify individual nanoparticle clusters from darkfield scattering images with high accuracy. With a rational assay design and simple synthesis procedure, this simple digital assay platform could be engineered for high-sensitivity protein target detection for disease diagnostics.

Introduction

Sensitive and accurate protein molecule detection is vital in biological and biomedical fields. For example, the detection of protein cancer biomarkers in serum or oral samples, also known as "liquid biopsy", provides a means for early diagnosis of cancer, which helps customize treatment plans for patients.[1–3] Moreover, sensitive antibody profiling of individuals could help monitor infectious diseases such as COVID-19 and determine the stage of disease progression,[4,5] which provides important epidemiological information for disease surveillance and control.[6] Although point-of-care (POC) assays such as lateral flow assays (LFAs) have recently become more commercially available,[7] the enzyme-linked immunosorbent assay (ELISA) remains the gold standard method for protein detection. However, drawbacks of ELISA, such as laborious blocking and washing steps, large sample volume, lower sensitivity than nucleic acid amplification assays, and expensive plate reader devices, restrict its broader applications.

Digital assays have emerged as a new assay design strategy in recent years, providing an easy-to-adopt approach to improve detection sensitivity for both protein and nucleic acid analyses. In contrast to traditional "analog" assays, where continuous signal intensity is measured from a bulk sample medium, digital assay signals are measured from spatially discrete compartments. By partitioning samples into a large number of small reaction chambers, each compartment is allowed to be loaded with "0" or "1" target molecule. The local enrichment effect increases the signal-to-noise ratio (SNR) in individual compartments, overcoming the low SNR challenges in conventional analog assays.[8–11] Protein detection can benefit significantly from digital assay technique as proteins cannot be easily amplified to multiple copies like nucleic acid targets. A number of protein-targeting digital assays have been previously developed using different partitioning configurations, including microbead-based compartments,[12–19] micro-bubbling,[20] water-in-oil droplets,[21] and microwells.[22,23] However, complex compartment generation methods, including microwells and microfluidic droplets, are inevitable in these assay techniques, limiting their applications in POC settings.

Plasmon coupling is one of the most studied sensing mechanisms for plasmon-resonant nanoparticles. As the distance between two plasmonic nanoparticles falls below around 2.5 times the particle diameter,[24] the plasmon modes

Department of Chemical and Biomolecular Engineering, North Carolina State University, Raleigh, NC 27695, USA. E-mail: qwei3@ncsu.edu

† Current address: College of Information and Electrical Engineering, China Agricultural University, Beijing, 100083, China.

© 2025 The Author(s). Published by the Royal Society of Chemistry

Open Access Article. Published on 28 July 2025. Downloaded on 11/2/2025 4:17:36 AM.
This article is licensed under a Creative Commons Attribution-NonCommercial 3.0 Unported Licence.

from each particle hybridize, which causes a redshift of the plasmonic peak of the coupled nanoparticle.[25,26] Plasmon coupling between nanoparticles significantly changes the spectroscopic profile of the nanoparticles in both peak wavelength and intensity. The fractional redshift of plasmonic peaks ($\Delta\lambda/\lambda_0$) can describe the relative strength of coupling, which decays exponentially as the distance increases.[27] The scattering intensity of the coupled nanoparticle dimer also increases due to the increased scattering cross-section. While plasmon coupling sensors are conventionally characterized by bulk analytical methods such as spectroscopy[28] or color measurement[29] of the ensemble nanoparticles, these optical changes have also been measured recently by single-nanoparticle imaging or spectroscopy measurements to improve detection sensitivity.[30–33] However, direct correlation of the number of plasmon-coupled nanoparticles to target concentration is rarely reported.

By combining plasmonic nanoparticles and single-particle counting, we propose a novel digital assay based on surface-confined reactions. This new digital plasmon coupling assay can be performed in bulk solution without the need for complex microfluidic droplet generation or microwell chip fabrication. After the reaction, the coupled nanoparticles can be deposited on glass slides for single-particle digital counting. In this design, the surface of the nanoparticle is essentially the compartment unit, where surface reactions such as antibody–antigen binding can occur. In the presence of target molecules, the surface ligands of two nearby nanoparticles can capture the same target and form an immunocomplex. As the surface reaction occurs only at the interface of two nanoparticle surfaces, this strategy works in the same way as other digital assays that partition the entire reaction volume into small, discrete compartments. For quantification, coupled nanoparticles where reactions occur will be regarded as positive or "1" signal, while single nanoparticles with no surface reactions will be regarded as negative or "0" signal. As the number of surface reactions on the nanoparticles increases, the coupled nanoparticle population will also increase.

In this work, we demonstrated a proof-of-concept digital plasmonic assay based on the plasmon coupling effect between silver (Ag) and gold (Au) nanoparticles (NPs). Streptavidin–biotin interaction was used to mimic the antigen–antibody interaction. By facile and efficient physical adsorption of proteins, streptavidin–silver nanoparticles were synthesized and optimized for stability. Plasmon coupling reaction between streptavidin–silver (SA–AgNP) and biotin–gold nanoparticle (Bt–AuNP) was demonstrated *via* UV-Vis spectroscopy, darkfield microscopy, and electron microscopy. In addition, a systematic FDTD simulation study on the plasmonic shift for coupled nanoparticles with different nanoparticle sizes and material combinations was conducted to obtain the strongest signal enhancement from plasmon coupling. Finally, a counting algorithm was developed to fully quantify the color and, hence, different populations of nanoparticles from darkfield microscopy images. This simple and effective digital plasmonic assay platform may open up a wide range of prospective applications, such as high-sensitivity protein biomarkers, antibody detection, and disease diagnostics.

Results and discussion

Assay overview

The principle of the single-nanoparticle digital plasmonic assay is shown in Fig. 1. The assay consists of two types of plasmonic

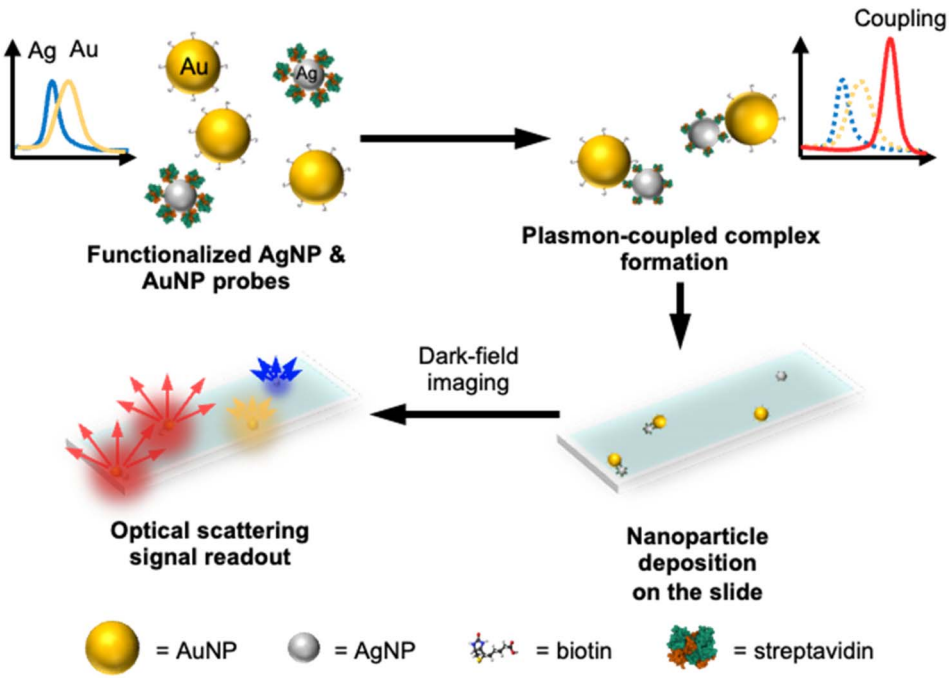

Fig. 1 Schematic of the digital plasmonic coupling assay based on streptavidin–biotin interaction.

Open Access Article. Published on 28 July 2025. Downloaded on 11/2/2025 4:17:36 AM. This article is licensed under a Creative Commons Attribution-NonCommercial 3.0 Unported Licence.

probes, Au NPs and Ag NPs, respectively. Au and Ag NPs were chosen due to their relatively large scattering cross-section, distinct resonant peaks under darkfield scattering conditions, and significant plasmonic coupling effect (also see the FDTD simulation section).[34,35] For a proof-of-concept, Au NPs are functionalized with biotin (Bt–AuNP) and Ag NPs are conjugated with streptavidin (SA–AgNP), respectively. The biotin–streptavidin interaction is used to construct a demonstration assay; however, this interaction can be replaced with biomarker-specific recognition ligands such as antibodies, peptides, or aptamers. When Bt–AuNP and SA–AgNP meet in the solution, Ag–Au complexes are formed guided by the streptavidin–biotin interaction. When the interparticle distance between the nanoprobes in the complex is 3–5 nm or smaller, plasmon overlap occurs, which changes the wavelength and intensity of the main plasmonic peaks of the extinction spectra. Darkfield microscopy can be used to easily detect the coupled nanoparticles by monitoring color changes, followed by a simple deposition of the coupled nanoparticles onto a glass slide. By counting the population of coupled particles and uncoupled particles, a relationship between particle amount and target concentration in the solution can be established.

Nanoparticle functionalization and optimization

Protein-conjugated plasmonic nanoparticles have been synthesized in many different ways.[36–38] The two dominant approaches include chemical conjugation and physical adsorption.[39–41] Chemical conjugation permanently links the nanoparticle surface with the functional groups in the protein, such as carboxyl, amine,[42,43] and thiol[44] groups. On the other hand, physical adsorption or passive adsorption relies on physical interactions between the protein and the surface of the nanoparticle, including electrostatic or hydrophobic interactions. In this work, one-step functionalization of silver nanoparticles was achieved by physical adsorption of SA onto citrate-capped Ag NPs. Similar to other proteins, we believe SA spontaneously adsorbs on the surface of Ag NPs, mainly through electrostatic and hydrophobic interactions.[45–47] The plasmonic peak of the Ag NPs shifted from 419 nm to 426 nm after adsorption of SA, indicating a change in the local refractive index and hence successful conjugation with SA (Fig. S1a).

It is important to obtain uniform and stable Ag NP conjugates and prevent them from agglomeration during the synthesis and purification, and before reaction with other plasmonic nanoparticles. However, we found that maintaining the stability of SA–AgNPs during centrifugation poses a significant challenge. Significant agglomeration and aggregation were observed by UV-Vis spectroscopy after removing SA–AgNPs from the protein reaction mixture by centrifugation (Fig. S1b). Darkfield scattering imaging also revealed the aggregation of SA–AgNPs after centrifugation. Instead of the characteristic blue color from single Ag NPs, the aggregates exhibit yellow to orange scattering color owing to broadening of the resonant scattering peak into the longer wavelength range (Fig. S1c and d).

To optimize protein adsorption and nanoparticle stability, we investigated different experimental conditions, including conjugation time, stoichiometric ratio of reagents, and the effect of stabilizing agents such as bovine serum albumin (BSA). First, we found that the reaction time did not significantly affect the nanoparticle stability up to 60 minutes. The peak wavelength and absorption (Abs) remained relatively stable over 60 minutes of adsorption and decreased thereafter (Fig. S2a and b). To maximize SA adsorption on the Ag NP surface while minimizing peak absorption reduction, a reaction time of 60 minutes was adopted for all subsequent experiments.

Interestingly, we found that higher amounts of SA resulted in lower stability of SA–AgNP after centrifugation. When 1 mg per mL SA (18.18 μM) was added to the OD2.5 AgNP solution (42.6 pM), with the SA volume increased from 0.5 to 10 μL (corresponding to 95 to 1652 nM) in the reaction mixture, the absorption peak of SA–AgNP widened and the peak absorption value decreased after purification (Fig. 2a and S3a). It should be noted that SA is always in a large excess compared to AgNP in all the controls (SA/AgNP molar ratio ranging from 2123 : 1 to 42477 : 1) (Fig. S1). We calculated the normalized decrease in peak absorption (normalized ΔAbs), where

$$\text{Normalized } \Delta\text{Abs} = \frac{\Delta\text{Abs}}{\text{Abs}@\lambda_{\text{peak,before}}} \times 100\%$$

This value was used to quantitatively describe the stability of the SA–AgNPs. Smaller normalized ΔAbs values after centrifugation indicate more stable SA–AgNPs. Fig. 2b shows increasing normalized ΔAbs with increasing amounts of SA added from 0.5 μL to 10 μL. When 20 μL of SA is added, the normalized ΔAbs is less than that with 10 μL SA but still higher than that with lower SA concentrations. The high nanoparticle instability induced by SA concentration is attributed to the protein corona effect, where excess protein leads to protein denaturation and a reduction in the surface charge on the nanoparticles, ultimately contributing to nanoparticle aggregation.

To address this issue, we examined the use of BSA as a blocking agent together with SA. BSA has been widely used in molecular assays to passivate surfaces and reduce nonspecific adsorption of proteins.[48–50] BSA has also been used to stabilize gold nanoparticles and prevent aggregation under high ionic strength.[51] The quantity of additional BSA added was chosen to be 50% and 100% of the SA. With BSA added, the UV-Vis spectra of SA–AgNP after centrifugation became less widened than those with no BSA controls (Fig. S3b and c). Fig. 2c and d show that with 50% and 100% BSA added, both ΔAbs and normalized ΔAbs from both groups are lower than those without BSA. The use of 100% BSA resulted in slightly higher stability than with 50% BSA at lower SA amounts (below 5 μL). These results indicate that the addition of BSA enhanced the stability of SA–AgNP after centrifugation. The normalized ΔAbs under all conditions (with and without BSA) are compiled in the heatmap shown in Fig. 2e for better visualization and comparison. Based on these results, we found that adding 0.5 μL SA solution and 100% BSA provided the best result. We also found that adding BSA did not affect the aforementioned reaction time to achieve maximized SA adsorption (Fig. S2c–f). These results confirm that BSA can effectively stabilize the nanoparticles, even under

 © 2025 The Author(s). Published by the Royal Society of Chemistry

Open Access Article. Published on 28 July 2025. Downloaded on 11/2/2025 4:17:36 AM.
This article is licensed under a Creative Commons Attribution-NonCommercial 3.0 Unported Licence.

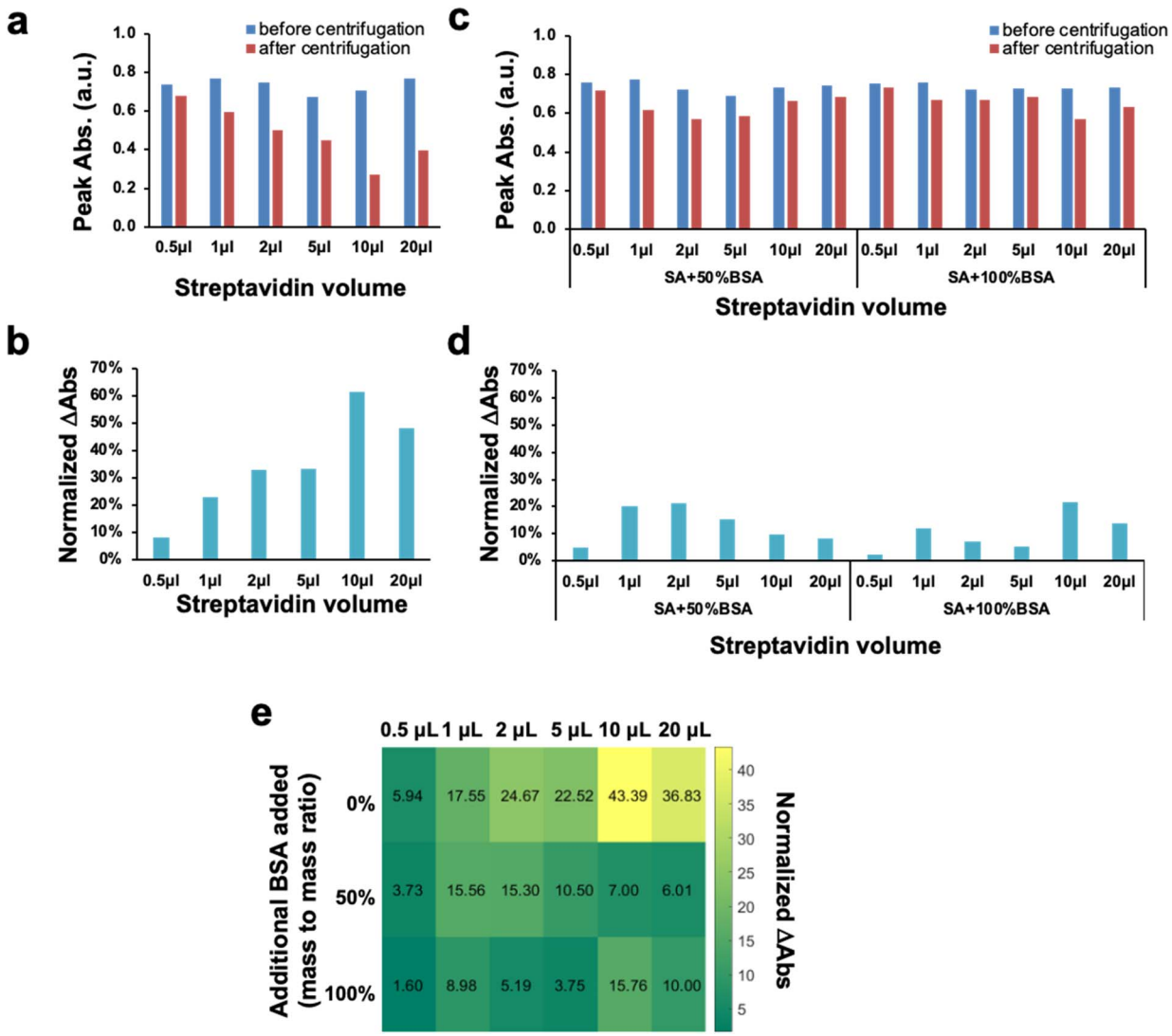

Fig. 2 Effect of SA and BSA adsorption on Ag NP stability. (a and b) Peak absorptions and normalized decrease in peak absorption (normalized ΔAbs) of SA–AgNPs before and after centrifugation, as assessed by UV-Vis measurement, with different amounts of SA added. (c and d) Effect of BSA on peak absorptions and normalized ΔAbs before and after centrifugation, as assessed by UV-Vis measurement. (e) Heatmap of normalized ΔAbs for different amounts of SA and BSA after centrifugation.

excess SA. Compared to previous blocking protocols with a typical final BSA concentration of approximately 1%, a much lower BSA concentration of 0.00025% (or 37.4 nM) was used in this work without significantly affecting the results.[52,53]

The SA–AgNP conjugates were also characterized with other methods in addition to UV-Vis spectroscopy. Dynamic light scattering (DLS) measurements showed that SA–AgNPs retained a well-dispersed narrow size distribution (PDI < 0.25) after centrifugation when a low concentration of SA was used (*e.g.*, 0.5 μL per 100 μL of Ag NPs, or final SA concentration of 60.6 nM) with or without BSA (Fig. 3a). The average hydrodynamic diameter, calculated either from the number weighted-mean (Num-averaged) or scattering intensity-weighted mean (*Z*-averaged), increases with increasing amounts of BSA (Fig. 3b). Similarly, the zeta potential also increases with increasing amounts of BSA (Fig. 3c). These results can be attributed to the formation of a protein corona surrounding the Ag NPs. TEM images (inset of Fig. 3a) show that SA–AgNP remains dispersed after purification, which is consistent with the DLS (Fig. 3a) and UV-Vis results (Fig. S3).

In order to further understand the adsorption of streptavidin on Ag NPs, we fitted the shifted wavelength using the Langmuir adsorption model ($R^2 = 0.92$) (Fig. S4) in the same way as reported in previous studies.[54–58] Because SA is in large excess (*ca.* 10^3–10^6 times) over AgNP, it can be assumed that the initial concentration of SA can be regarded as the equilibrium concentration. The highest SA concentration was not included in the fitting because the plasmonic peak no longer redshifts, meaning the adsorption has saturated. The binding constant between SA and 50 nm Ag NP was calculated to be 3.4×10^7 M^{-1}. The value was on the same order of magnitude as other binding constants for protein–AgNP[54,55] and protein–AuNP.[57]

Open Access Article. Published on 28 July 2025. Downloaded on 11/2/2025 4:17:36 AM.
This article is licensed under a Creative Commons Attribution-NonCommercial 3.0 Unported Licence.

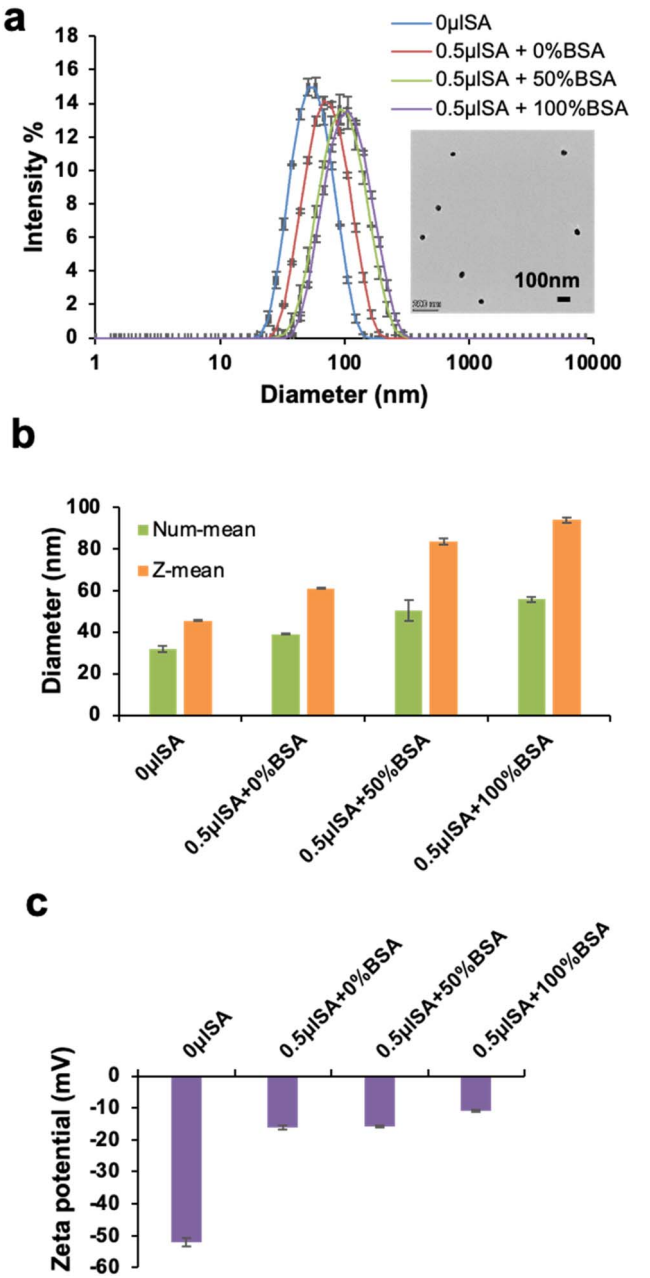

Fig. 3 Characterization of SA–AgNPs with optimized SA amount. (a) *Z*-Averaged size distribution for Ag NPs before and after SA adsorption and purification, measured by DLS. PDI for size distribution were 0.24, 0.21, 0.18, and 0.17. Inset: TEM image of SA–Ag NP with 50% BSA. (b) Num-averaged and *Z*-averaged sizes for silver NPs before and after SA adsorption and purification. For the DLS measurements, the Ag NPs were diluted 10 times from the stock solution/reaction mixture, yielding a final concentration of 4.28 pM (Ag NP) and 2.85 pM (SA–AgNP). (c) Zeta potential for Ag NPs before and after SA adsorption and purification.

However, it is noteworthy that large discrepancies exist between reported protein-nanoparticle binding constants measured with different approaches.[59]

The maximum spectral peak shift can also be used to estimate the thickness of the adsorbed layer on the nanoparticle surface. The maximum wavelength shift ($\Delta\lambda_{max}$) is proportional to the change in the local refractive index and can be estimated from the following equation:

$$\Delta\lambda_{max} = m(n_{ads} - n_{medium})\left(1 - e^{-\frac{2d}{l_d}}\right)$$

where m is the refractive index (RI) sensitivity, n_{ads} and n_{medium} are the refractive indexes for the adsorbate and medium, respectively, and d and l_d are the thickness of the adsorbed layer and the characteristic length, which depends on the material, respectively.[60,61] The equation describes the wavelength response to local refractive change in LSPR sensors. The RI sensitivity m depends on the size, material, and surface ligand of nanoparticles.[62] For 50 nm AgNPs, the m has been reported to range from approximately 160 nm^{-1} (ref. 63 and 64) to 200 nm^{-1}.[62] For estimation, the RI sensitivity value m was taken as 160, adsorbate RI as 1.45 (SA),[65] medium RI as 1.33 (water), and the characteristic decay length as 6 nm.[60] With these values, the adsorbed layer thickness d can be calculated as 1.77 nm from the experimental data. From the literature, the adsorbed protein monolayer thickness varies from 1.45 nm to 6 nm in different studies.[66] Our estimated layer thickness (1.77 nm) thus matches well with literature values. Based on both Langmuir adsorption fitting and protein absorption layer thickness estimation, we conclude that the monolayer adsorption model is effective in describing the adsorption of SA molecules on Ag NPs in our case.

Based on the adsorption model, we proposed plausible reasons for SA-induced aggregation of nanoparticles, especially at high SA concentrations. Previous studies showed that higher concentrations of proteins could induce nanoparticle aggregation, during which the protein conformation changes.[67,68] In this theory, protein molecules unfold on the nanoparticle surface and could serve as crosslinkers between nanoparticles, leading to irreversible aggregation. Under higher SA concentrations, we conclude that SA–AgNPs underwent similar dynamics, leading to AgNP aggregation. As the SA amount increased to 20 μL, we noted a decrease in normalized ΔAbs, indicating slightly improved nanoparticle stability (Fig. 2b). A possible reason could be that SA has already reached saturation adsorption on the Ag NP surface at a volume of approximately 10 μL SA. Introduction of more SA leads to the formation of a multilayer protein corona instead of monolayer adsorption. The multilayer protein corona reduced the probability of protein denaturation for the outermost layer of proteins, thereby reducing the crosslinking and aggregation of the nanoparticles.

BSA has been found to bind with metallic nanoparticles in many ways, including hydrophobic interaction,[51] metal–sulfur coordination,[69] and electrostatic interaction.[70] As BSA has an isoelectric point (pI) between 4.7 and 5.1,[71] and is negatively charged in neutral solutions, hydrophobic interaction and metal coordination could be more dominant forces than electrostatic interaction in its binding with citrate-capped Ag NPs, which are also negatively charged. BSA could occupy the vacant adsorption sites on Ag NPs and reduce the high-density

 © 2025 The Author(s). Published by the Royal Society of Chemistry

Open Access Article. Published on 28 July 2025. Downloaded on 11/2/2025 4:17:36 AM.
This article is licensed under a Creative Commons Attribution-NonCommercial 3.0 Unported Licence.

adsorption of SA, acting as a blocking agent on the nanoparticle surface. Therefore, BSA can reduce the nonspecific adsorption of SA–AgNPs onto the tubes or form hard pellets at the bottom of the tube under strong *g*-force during centrifugation (Fig. S5).

It is interesting to note that although SA and BSA have similar molecular weights, their influence on Ag NP stability differs. The difference in charge between SA and BSA might play a role in the different adsorption behaviors. The recombinant SA we used has a neutral isoelectric point (pI) of 6.8, while BSA has a lower pI of between 4.7 and 5.1.[71] As such, BSA is slightly more negatively charged than SA under neutral conditions. A more negatively charged nanoparticle surface could generate a stronger repulsive force between nanoparticles than between neutrally charged surfaces.[72] Although the binding constants between SA–AgNP and BSA–AgNP systems were not measured in this work, further studies could focus on the cooperative adsorption mechanism and dynamics of SA and BSA binding on metallic nanoparticles using fluorescence quenching spectroscopy methods.[59]

In addition to adding BSA, the formation of a hard pellet and nanoparticle aggregation could also be avoided by reducing the nanoparticle concentration during centrifugation (Fig. S6) or adding surfactants (Tween 20) to the reaction mixture before centrifugation (Fig. S7). Both methods reduced both plasmonic peak broadening and absorption peak decrease after centrifugation, which was validated by both UV-Vis spectroscopy and darkfield scattering microscopy. While adding surfactants further improved the nanoparticle dispersity, we found that simply reducing the nanoparticle concentration is sufficient to prevent nanoparticle aggregation, without possible interference on the surface reactivity of nanoparticles from the adsorbed surfactant molecule. Finally, in addition to using citrate-capped Ag NPs, which may be susceptible to oxidation and pH, highly stable and robust Ag NPs have also been synthesized,[73–75] which could be used in the future to address the stability issue.

Demonstration of the digital plasmonic coupling assay

The proof-of-concept of the digital plasmon coupling assay was carried out using SA–AgNPs previously synthesized with Bt–AuNPs. The strong affinity and mild reaction conditions between streptavidin–biotin make it ideal for mimicking the antigen–antibody interaction for protein detection. Most commercially available biotinylated nanoparticles use a long PEG chain as the linker between the biotin and the nanoparticle.[76,77] While this strategy increases the stability of the nanoparticles, the PEG linker is too long for plasmon coupling to occur. Instead, we chose a Bt–AuNP probe with a short linker of only four carbon atoms between biotin and gold. Fig. 4a shows the extinction spectra of dispersed SA–AgNPs and Bt–AuNPs, exhibiting their characteristic plasmonic peaks at 426 nm and 571 nm, respectively. Darkfield scattering microscopy confirmed the good dispersity of both silver and gold

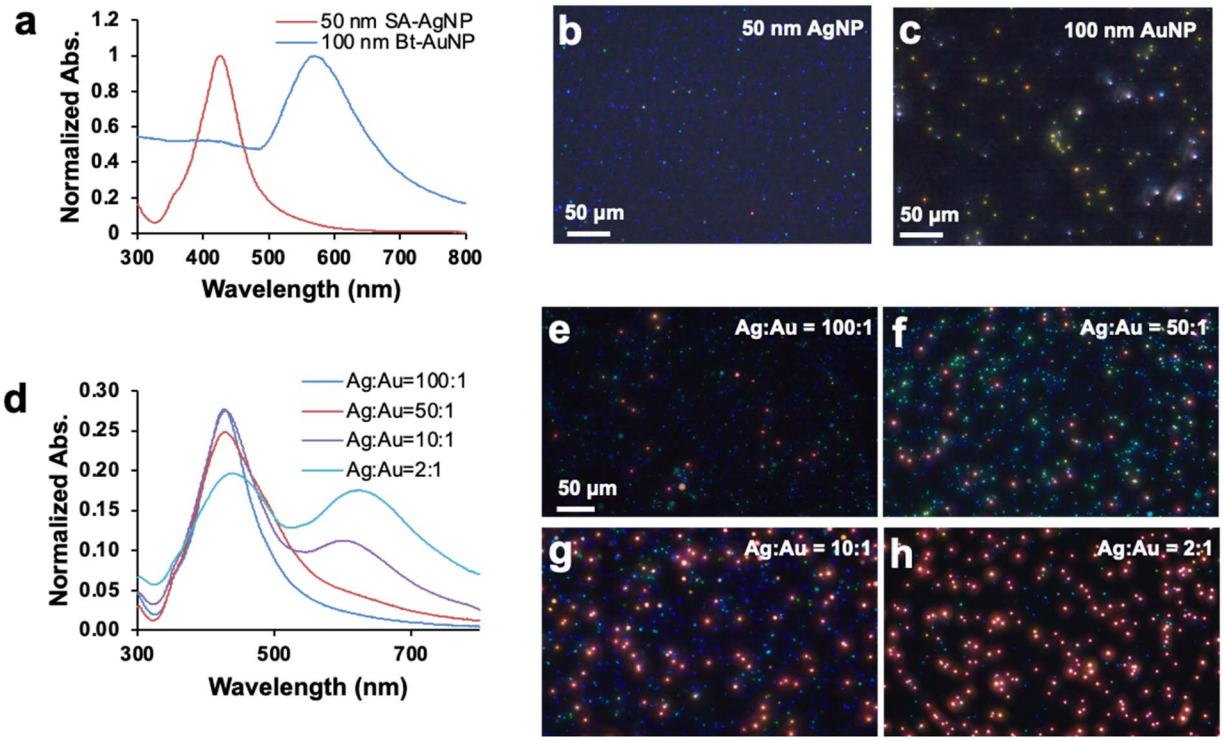

Fig. 4 Plasmon-coupling between SA–AgNPs and Bt–AuNPs. (a) Normalized UV-Vis spectra of 50 nm SA–AgNPs and 100 nm Bt–AuNPs before the plasmon coupling reaction. (b and c) Darkfield scattering images of 50 nm SA–AgNPs and 100 nm Bt–AuNPs before reaction. (d) Normalized UV-Vis spectra of 50 nm SA–Ag NPs and 100 nm Bt–AuNPs after the plasmon coupling reaction. The molar ratio of AgNP/AuNP ranges from 100 : 1 to 2 : 1. (e–h) Darkfield scattering images of Ag–Au mixtures at different molar ratios of AgNP/AuNP (100 : 1, 50 : 1, 10 : 1, to 2 : 1). All nanoparticles were dispersed in water.

Open Access Article. Published on 28 July 2025. Downloaded on 11/2/2025 4:17:36 AM.
This article is licensed under a Creative Commons Attribution-NonCommercial 3.0 Unported Licence.

nanoparticles in the solution (Fig. 4b and c). The blue scattering color from single SA–AgNPs and yellow-green scattering color from Bt–AuNPs match their plasmonic peaks with the UV-Vis results. For assay demonstration, different amounts of Bt–AuNPs were mixed with the SA–AgNPs (Ag/Au molar ratio = 100 : 1 to 2 : 1). When the St–AuNPs were introduced, a new plasmonic peak appeared at around 630 nm, indicating the plasmonic coupling between gold and silver nanoparticles (Fig. 4d). As more Bt–AuNPs were added to the SA–AgNPs mix, this new plasmon coupling peak increased in intensity (Fig. 4d). Darkfield scattering microscopy further confirmed the formation of new nanoparticle clusters (Fig. 4e–h). A new population with a distinct pink-red scattering color emerged from the blue colored background of single BA–AgNPs when increasing amounts of Bt–AuNPs were introduced (Fig. 4e–h). The plasmon-coupled nanoparticles were brighter than both single SA–AgNPs and Bt–AuNPs. In contrast, in the control experiment using unfunctionalized Ag NPs and Au NPs, the nanoparticles retained their original scattering color as single particles, meaning neither surface reaction nor plasmon coupling between gold and silver nanoparticles occurred (Fig. S8). The nanoparticle solution sample can also be completely dried out for easy counting. Despite the slight scattering color difference due to the different refractive indices of water *versus* air, the conclusion remained the same: the relative amount of plasmon-coupled particles increased as more Bt–AuNPs were added to the SA–AgNPs. No color change was observed for the control groups (without surface functionalization) after mixing (Fig. S9 and S10).

To further validate the formation of nanoclusters between SA–AgNPs and Bt–AuNPs, we obtained electron microscopy images for individual and plasmon-coupled gold and silver nanoparticles (Fig. 5). From transmission electron microscopy (TEM) images, we observed the assembling of larger gold and smaller silver NPs (Fig. 5a and b). The distance (*ca.* 3–5 nm) between gold and silver nanoparticles in Fig. 5b is sufficiently small for plasmon coupling to occur. Electron dispersive X-ray spectroscopy (EDS) analysis was also carried out to identify the elemental composition of the nanoparticle clusters. It is clear that the silver element distribution overlapped with smaller nanoparticles while the gold element distribution overlapped with larger nanoparticles (Fig. 5c). The EDS spectrum showcased the characteristic energy peaks for silver and gold, respectively (Fig. 5d). More plasmon-coupled nanoparticles could be observed from larger field of view (FOV) TEM images (Fig. S11a), while no plasmon-coupled nanoparticles were observed in the control group without surface functionalization (Fig. S11b).

We also performed scanning electron microscopy (SEM) and darkfield scattering microscopy from the same region of interest (ROI) to correlate darkfield scattering color with actual nanoparticle structures (single or cluster) (Fig. 5e–g). Fig. 5e and f show the same ROI from darkfield scattering microscopy and SEM. The zoomed-in SEM images (Fig. 5g) show four nanostructures contributing to particle scattering in Fig. 5e. Only the particle in image Fig. 5g(2) is a single Ag NP as revealed by the SEM image, corresponding to the blue color in the darkfield scattering; the other three are Au–Ag clusters, with

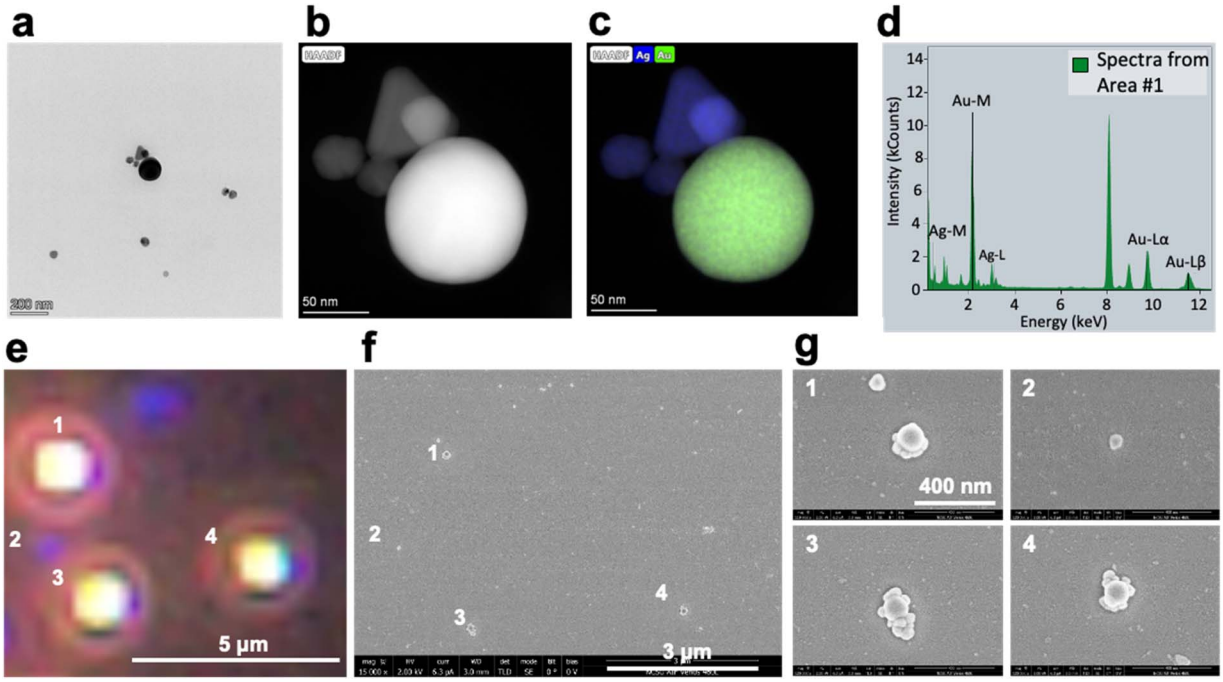

Fig. 5 TEM and SEM characterization of plasmon-coupled silver and gold nanoparticles. (a) TEM, (b) STEM, and (c) EDX images of plasmon-coupled silver and gold nanoparticles. (d) EDX elemental analysis shows characteristic X-ray peaks from silver and gold nanoparticles. (e) Darkfield scattering and (f) SEM image of plasmon-coupled silver–gold nanoparticles from the same region of interest. (g) Zoomed-in SEM images of individual nanocomplexes from regions 1–4 in (f).

 © 2025 The Author(s). Published by the Royal Society of Chemistry

Open Access Article. Published on 28 July 2025. Downloaded on 11/2/2025 4:17:36 AM.
This article is licensed under a Creative Commons Attribution-NonCommercial 3.0 Unported Licence.

characteristic pink-red scattering color in the darkfield due to plasmonic coupling. We systematically studied the relationship between nanoparticle color in the darkfield scattering images and nanoparticle morphology as confirmed by SEM, the results of which are summarized in Fig. S12. We conclude that blue-, cyan- and green-colored nanoparticles represent single Ag NPs or oligomers of 50 nm Ag NPs. Brighter yellow-colored nanoparticles are 100 nm Au NPs. The nanoparticles with the highest brightness on the image are plasmon-coupled Au–Ag nanoparticles, which have the highest scattering intensity and longest scattering wavelength among all nanoparticles. This color map is used to classify different populations of nanoparticles in the counting step. To summarize, UV-Vis spectroscopy, darkfield optical microscopy, and electron microscopy studies demonstrated the assembly and plasmonic coupling between SA–AgNPs and Bt–AuNPs mediated by the surface reaction of streptavidin and biotin.

FDTD simulation of plasmonic coupling

As a classic theory in light–nanoparticle interaction, Mie theory has been used to predict the optical properties and calculate the extinction, absorption, and scattering spectra of nanoparticles that matched well with experimental results.[78,79] However, the difficulty of calculating the optical spectra for more complex geometry, such as dimers and clusters, limited its application in this study. Finite-difference time-domain (FDTD) is a powerful computational method to simulate the electromagnetic field in nanophononics, especially for plasmonic materials.[78,80] In this method, Maxwell's equation is solved on a spatial grid. Absorption and scattering spectra can be simulated by applying the Fourier transform to the time-dependent fields. We performed FDTD simulation to predict the plasmonic coupling effect and, more importantly, to prove Ag–Au pairs would generate larger red-shifts after coupling than Ag–Ag or Au–Au combinations.

To begin with, the scattering, absorption, and extinction spectra for single gold and silver nanoparticles were first simulated using both Mie theory calculations and FDTD simulations (Fig. S13). The accuracy of the FDTD simulation was validated by comparing the spectra with those calculated from Mie theory, including peak position and peak shape. The results show that the two methods agreed very well (Fig. S13). As the Ag and Au NP size increases, the scattering component becomes more dominant in the extinction spectra (Fig. S13c and d). For larger nanoparticles, multiple peaks appear, corresponding to dipole and quadrupole plasmonic modes.[81]

We then simulated the scattering spectra (Fig. 6a) and the extinction spectra (Fig. 6b) for a single 50 nm Ag NP, a single 100 nm Au NP, and Ag–Au dimers. Here, the dimer is chosen as

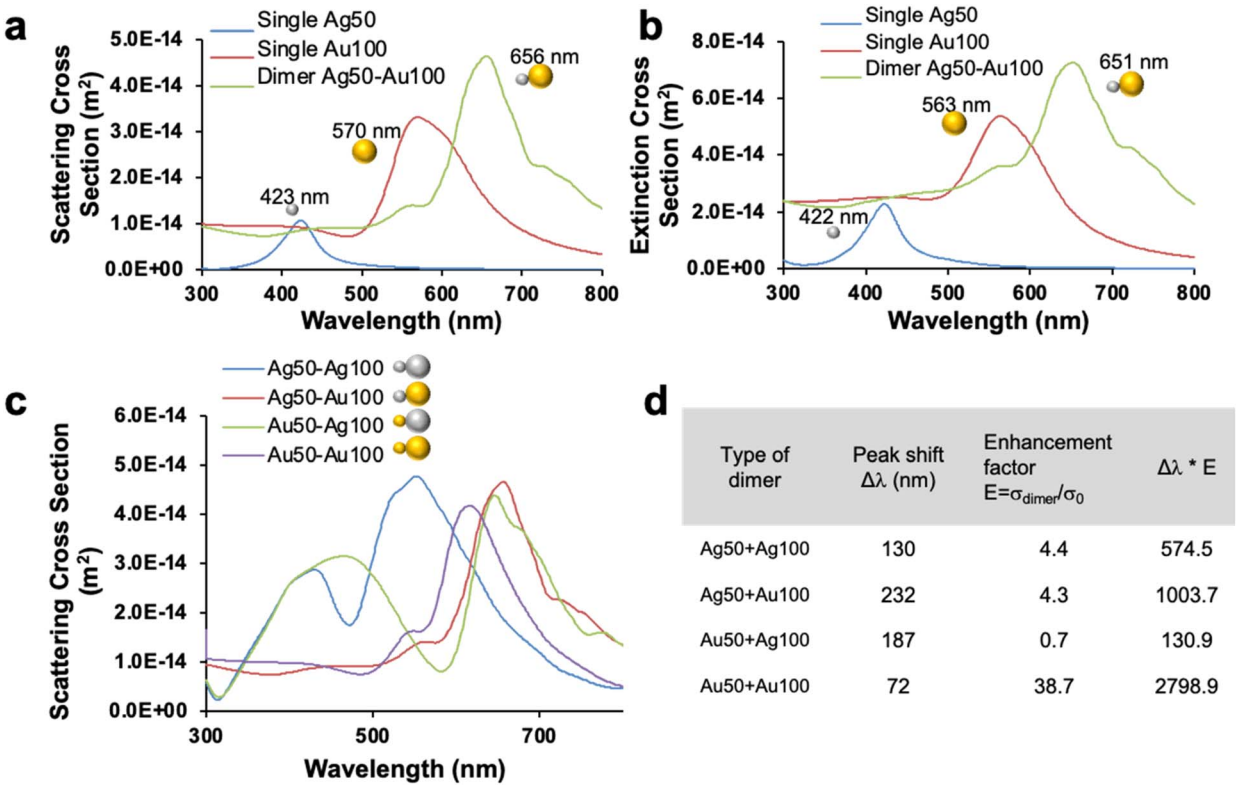

Type of dimer	Peak shift Δλ (nm)	Enhancement factor $E=\sigma_{dimer}/\sigma_0$	Δλ * E
Ag50+Ag100	130	4.4	574.5
Ag50+Au100	232	4.3	1003.7
Au50+Ag100	187	0.7	130.9
Au50+Au100	72	38.7	2798.9

Fig. 6 FDTD simulation of plasmon coupling between silver and gold nanoparticles. (a) FDTD simulated scattering spectra of a single 50 nm AgNP, single 100 nm AuNP, and a dimer of Ag50–Au100; (b) FDTD simulated extinction spectra of a single 50 nm Ag NP, single 100 nm AuNP, and a dimer of Ag50–Au100; (c) FDTD simulated scattering spectra of four representative combinations between 50 nm and 100 nm silver/gold nanoparticles; (b) summarized analysis of the simulated scattering spectra for four combinations between 50 nm silver/gold and 100 nm silver/gold nanoparticles. Water was used as a medium for all simulations ($n = 1.33$).

Open Access Article. Published on 28 July 2025. Downloaded on 11/2/2025 4:17:36 AM.
This article is licensed under a Creative Commons Attribution-NonCommercial 3.0 Unported Licence.

a simple model for plasmonic coupling. The plasmon-coupled dimer exhibited redshifted resonant wavelengths and increased intensity compared to single nanoparticles (green curves, Fig. 6a and b). In particular for the scattering spectra, the plasmon-coupled Ag–Au dimer exhibited a new plasmonic peak at 656 nm, the scattering intensity of which was approximately 4.5 and 1.3 times stronger than the single Ag and Au nanoparticles, respectively (Fig. 6a). The simulated scattering properties are consistent with the darkfield scattering microscopy results, in which Ag–Au nanoclusters exhibited a bright red-pink color (Fig. 4h).

To provide more insight into the rational selection of the nanoparticle size and composition of the gold/silver nanoparticles, we performed a thorough FDTD analysis of the scattering spectra of plasmon-coupled nanoparticle dimers with different combinations of gold and silver nanoparticles (ten combinations in total, see Table S2 and Fig. S14). Fig. 6c and d show the FDTD results of four of the ten combinations of 50 nm and 100 nm nanoparticles we simulated. For quantitative comparison, we focus on two parameters that can describe the degree of plasmon coupling; namely: (1) wavelength shift ($\Delta\lambda = \lambda_{\text{dimer}} - \lambda_0$, where λ_0 is the starting plasmonic wavelength of individual Ag or Au NPs), and (2) peak intensity enhancement factor ($E = \sigma_{\text{dimer}}/\sigma_0$, where σ_0 is the starting peak cross section of individual Ag or Au NPs). A large peak shift $\Delta\lambda$ is beneficial for color visualization, while a large enhancement factor E is beneficial for single-particle detection from background scattering noise. To take both factors into account, the product $\Delta\lambda \times E$ is calculated for each combination. Both Ag50/Au100 and Au50/Au100 combinations have large $\Delta\lambda \times E$ (Fig. 6d). However, although the Au50/Au100 combination yields a larger value in the product, this is largely due to the very low scattering intensity of 50 nm Au NPs. For real applications, the weak scattering of 50 nm Au NPs would complicate single-particle imaging. Moreover, the Au50/Au100 combination only exhibited a plasmonic shift of 72 nm in peak wavelength, which is the smallest among the four combinations (Fig. 6d). In contrast, the combination of Ag50/Au100 showed the largest scattering wavelength shift and also relatively high scattering intensity enhancement. A complete analysis for all ten possible combinations between 50 nm and 100 nm gold and silver nanoparticles is summarized in Fig. S14 and Table S2. The conclusion still holds true that the Ag50–Au100 combination provides the largest peak shift and second-largest enhancement among all the combinations. The greater spectral coupling of Ag–Au than the Ag–Ag or Au–Au homodimer is attributed to the formation of hybrid plasmonic modes due to asymmetric charge distribution between Ag and Au and therefore a larger energy splitting (wavelength shift) than symmetric dimmers. The simulation results not only match with the experimental

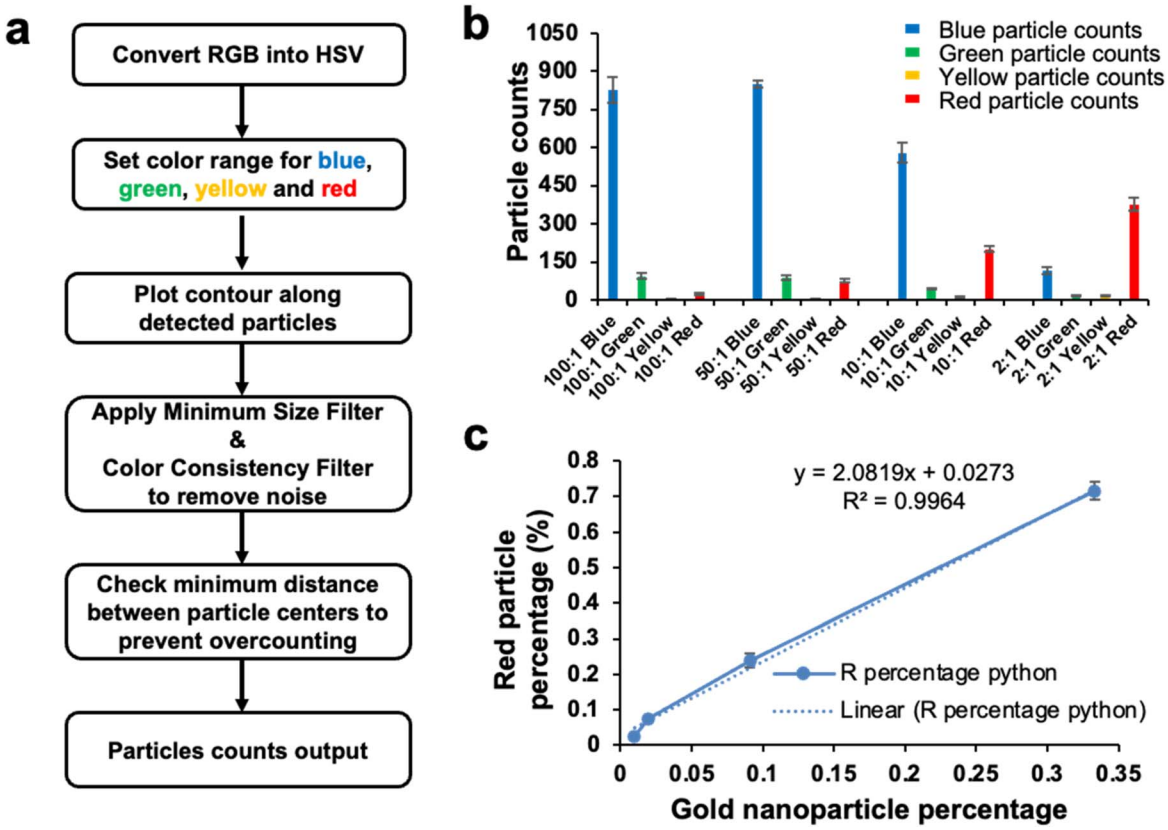

Fig. 7 Single-particle counting for the digital plasmonic coupling assay. (a) Flowchart of the counting algorithm for quantification of different types of nanoparticles based on darkfield scattering microscopy images. (b) Blue, green, yellow, and red particle counts from darkfield scattering microscopy images with different silver to gold molar ratios. (c) Linear fitted relationship between the percentage of gold nanoparticles in the reaction mixture and the percentage of red particles counted in the image.

 © 2025 The Author(s). Published by the Royal Society of Chemistry

Open Access Article. Published on 28 July 2025. Downloaded on 11/2/2025 4:17:36 AM.
This article is licensed under a Creative Commons Attribution-NonCommercial 3.0 Unported Licence.

observations but also explain why the Ag–Au pair was chosen for the digital plasmonic coupling assay.

Single-nanoparticle counting with darkfield scattering images

In the final step, the plasmon-coupled nanoparticles need to be accurately counted for target quantification. A well-developed image processing algorithm is key to the sensitive detection of plasmon-coupled nanoparticles. In previous studies on dark field microscopy-based assays, an automated particle recognition and counting algorithm was developed.[33,82,83] For our assay platform, we also developed a particle-counting algorithm in the Python environment. Based on the color map developed previously (Fig. S12), our code detects and counts four colors: blue, green, yellow, and red. These four colors correspond to single silver, silver oligomer, single gold, and gold–silver coupled nanoparticles, respectively.

As illustrated in the flow diagram in Fig. 7a, the RGB scattering images were first converted into HSV color space to minimize the difference in lighting conditions and exposure settings during image acquisition. Hue, saturation, and threshold values were then optimized and determined for each of the four colors. With the color threshold, a mask was generated containing all identified nanoparticles. Contour lines were then drawn outside the detected particles for visualization. A minimum-size filter was added to expel noise dots from the total particle population. Similarly, color consistency was calculated so dots with too much color variance were also discarded as noise. Finally, a minimum-distance filter was added to prevent double counting. In the case of double counting, the distance between two counted particles is too small to be counted as two particles. Fig. 7b shows the particle counting result from the image set shown in Fig. 4e–h. The percentage of red particles (Ag–Au coupled clusters) increased as the Ag/Au ratio decreased from 100 : 1 to 2 : 1. We then plotted the percentage of red particles as a function of the percentage of Au NPs in the nanoparticle mixture (Fig. 7c). A good linear relationship was observed between the counted red particle percentage and the Au NP percentage in the reaction mixture. One hypothesis is that all the Bt–AuNPs reacted with SA–AgNPs since Ag NPs are always present in excess in the mixture. The result shown in Fig. 7c indicates that the red particle percentage is an accurate indicator of the population change of plasmon-coupled nanoparticles in the mixture. The LOD on detecting biotinylated gold nanoparticles was estimated to be 107.5 fM (100 : 1 group). Although a small portion of Ag NPs agglomerated during the preparation of the sample, this did not affect the linearity of the fitted curve and thus the validity of the quantification results from this analytical method. Images from dry samples were also quantified using a similar counting algorithm (Fig. S15). Similarly, the red particle percentage is an effective indicator for plasmon-coupled nanoparticles.

Conclusion

In this study, we have demonstrated the feasibility of constructing a digital plasmonic coupling assay by single-particle imaging and counting. This new digital assay format removes the need for sophisticated microarray chip fabrication or droplet generation in conventional digital assays. Instead, the assay can be easily run in the bulk solution and later deposited on glass slides for digital readout. Using streptavidin and biotin as proof-of-concept, we developed a model assay using 50 nm Ag NPs and 100 nm Au NPs functionalized with streptavidin and biotin, respectively. Both scattering wavelength shift and scattering intensity increase of the coupled Ag–Au nanoclusters are observed, making it a promising assay platform for highly sensitive detection. We investigated in detail the stability of the protein-coated nanoparticles and observed different effects of SA and BSA in promoting nanoparticle stability. We also demonstrated the rational selection of Ag–Au pairs by a systematic simulation of the scattering spectra of coupled dimers using FDTD. A robust single-particle counting algorithm based on color recognition was also developed in Python. The system could be further extended to antibody–antigen interactions in the future, for real sensing applications.

Methods

Synthesis of streptavidin-conjugated silver nanoparticles (SA–AgNP)

0.5–20 μL of 1 mg per mL streptavidin (Thermo Fisher Scientific Inc.) solution was added to 100 μL of 50 nm citrate-capped silver nanoparticle solution (Cytodiagnostics Inc.) with an optical density (OD) of 2.5, and mixed in an Eppendorf tube. To synthesize bovine serum albumin (BSA) protected SA–AgNP, streptavidin and BSA (Sigma-Aldrich) solution were premixed at different ratios and added to the AgNP solutions. The reaction mixtures were left at room temperature for 80 min and then centrifuged at 4500 rpm for 20 minutes. After the supernatant was removed, the pellet was resuspended in 100 μL deionized (DI) water. Detailed reaction conditions and the final concentrations of reagents are listed in Fig. S1.

Formation of plasmon-coupled silver–gold nanoclusters

Biotin-conjugated 100 nm gold nanoparticles (Bt–AuNP) with a short 4C linker (Nanopartz) were diluted by 25× from the original concentrated stock solution. Then, different amounts of Bt–AuNP solutions were added to 100 μL SA–AgNP solution (OD = 0.83). The gold and silver nanoparticle mixed solutions were diluted to the same final volume of 125 μL with DI water. The reaction mixtures were incubated at room temperature for 2 hours with shaking.

UV-Vis spectroscopy and data analysis

The UV-Vis absorption spectra of the nanoparticle solutions were measured with a multimode plate reader (Varioskan LUX, Thermo Fisher). The typical measurement volume was 100 μL per well. Due to the difference in path length, the OD value from the plate reader was converted into the standard OD measured in a 10 mm cuvette by multiplying by a conversion factor (~3.2× of OD value from the plate reader) before converting into molar concentration. The decrease in peak absorption (ΔAbs) was

Open Access Article. Published on 28 July 2025. Downloaded on 11/2/2025 4:17:36 AM. This article is licensed under a Creative Commons Attribution-NonCommercial 3.0 Unported Licence.

calculated as the difference in absorption peak intensity before and after centrifugation:

$$\Delta\text{Abs} = \text{Abs}@\lambda_{\text{peak,before}} - \text{Abs}@\lambda_{\text{peak,after}}$$

The normalized decrease in peak absorption (normalized ΔAbs) was calculated as:

$$\text{Normalized } \Delta\text{Abs} = \frac{\Delta\text{Abs}}{\text{Abs}@\lambda_{\text{peak,before}}} \times 100\%$$

The following equation was used to fit the UV-Vis data of protein absorption into the Langmuir adsorption isotherm:

$$\theta = \frac{\Delta\lambda}{\Delta\lambda_{\max}} = \frac{Kc}{1 + Kc}$$

where θ is the surface coverage, $\Delta\lambda$ is the shifted absorption peak between protein-adsorbed AgNP and citrate-capped AgNP, K is the binding constant of the protein and AgNP, and c is the equilibrium concentration of the protein.

Darkfield scattering imaging

The sample for darkfield scattering imaging was prepared by adding 3 μL of diluted nanoparticle solution onto a glass slide, which was sealed with a coverslip. After settling the nanoparticles, darkfield images were recorded with an Olympus BX43 microscope with a 40× objective lens (Olympus, UPlanFLN, NA0.75), a dark field condenser (Olympus, U-DCW, NA1.2–1.4), and an Olympus DP74 color camera with a 0.63× C-mount adaptor. Images were acquired with CellSens Entry software with 100 ms exposure time and 16× gain. For dry samples, glass slides were plasma-treated for 30–60 s before nanoparticle solution application. The surface treatment promotes solution spread on the glass slide and therefore minimizes nonspecific nanoparticle aggregation due to the drying effect.

Dynamic light scattering (DLS) characterization

The size distribution and zeta potential were collected by DLS with a Malvern Zetasizer Nano-ZS particle size analyzer. Briefly, 1 mL of diluted nanoparticle solution was added to a standard cuvette and inserted into the cuvette holder. The scattering signal was obtained by the 173-degree back-scattering method.

Transmission electron microscopy (TEM) characterization

5 μL of diluted nanoparticle solution was added onto a TEM copper grid (01800, Ted Pella) and then extra liquid was wicked off with paper tissue. The TEM images were collected on a Thermo Fisher Talos F200X TEM using 200 kV acceleration voltage and a Thermo Ceta CMOS camera for imaging. Scanning transmission electron microscopy (STEM) imaging was performed at 200 kV acceleration voltage, using a high-angle annular dark field (HAADF) camera. Energy dispersive spectroscopy (EDS) data were also collected in STEM mode, using an EDS detector.

Scanning electron microscopy (SEM) characterization

The same glass slides used for darkfield scattering microscopy were completely dried before gold sputtering. Then, 5 nm gold–palladium (Au–Pd) was sputtered on the sample. The SEM images were collected on a FEI Verios 460L Field Emission SEM with 2 kV acceleration voltage and 13 pA beam current using a through-the-lens detector.

FDTD simulation

The finite-difference time-domain (FDTD) method was used to simulate the scattering, absorption, and extinction spectra for silver, gold, and coupled nanoparticles. The FDTD simulation was conducted using Ansys Lumerical software (version 2022 R2.1). The mesh size was set to be between 0.75 nm and 2 nm, depending on the size of the nanoparticles. The simulation time was set to 1000 fs at 300 K. An s-polarized (90° polarization angle) plane source with 300–1000 nm wavelength was used to study the absorption and scattering power cross-section responses. The refractive index of the surrounding media was set as 1.33 (water).

To calculate the scattering and absorption spectrum, scattering and absorption power were obtained first in the time domain. Briefly, the scattering power was calculated as the sum of the Poynting vector radial component integration from positive and negative x, y, and z directions of the simulation box. The absorption power was calculated as the opposite of the scattering summation. Both scattering and absorption cross section were obtained from the power by dividing by the incident intensity. Finally, the extinction cross-section was calculated as the sum of scattering and absorption cross-sections. To validate the effectiveness of the FDTD simulation, plasmonic spectra from Mie theory were also generated using the tool based on previous work.[84]

Single-nanoparticle counting algorithm

The algorithm for single-nanoparticle counting and color identification was developed in Python. Basically, each RGB raw image in TIF format from the microscope was converted into HSV space first. After thresholding using a predefined color map, particles with different colors could be extracted. The counted particles were further checked for size, distance to neighboring particles, and color consistency to ensure no particle was repeatedly counted. Around 500–1000 and 1500–2500 particles were counted from wet and dry samples, respectively.

Author contributions

S. Z. and Q. W. conceived the idea and designed the study. S. Z. and N. K. performed the experiments. S. J. performed the FDTD simulation of plasmon coupling. S. J. and Y. W. developed the single nanoparticle counting algorithm. S. Z. performed data analysis and wrote the manuscript. S. Z. and Q. W. revised the manuscript. All the authors participated in the discussion of results and have given approval to the final version of the manuscript.

 © 2025 The Author(s). Published by the Royal Society of Chemistry

Open Access Article. Published on 28 July 2025. Downloaded on 11/2/2025 4:17:36 AM.
This article is licensed under a Creative Commons Attribution-NonCommercial 3.0 Unported Licence.

Conflicts of interest

The authors declare no conflicts of interest.

Data availability

The data supporting this article have been included as part of the SI.

The supplementary information contains additional experimental data, images and simulation results. See DOI: https://doi.org/10.1039/d5na00403a.

Acknowledgements

This work was performed in part at the Analytical Instrumentation Facility (AIF) at North Carolina State University, which is supported by the State of North Carolina and the National Science Foundation (Award number ECCS-2025064). The AIF is a member of the North Carolina Research Triangle Nanotechnology Network (RTNN), a site in the National Nanotechnology Coordinated Infrastructure (NNCI).

References

1 C. A. Borrebaeck, Precision diagnostics: moving towards protein biomarker signatures of clinical utility in cancer, *Nat. Rev. Cancer*, 2017, **17**(3), 199–204.
2 T. N. Zamay, G. S. Zamay, O. S. Kolovskaya, R. A. Zukov, M. M. Petrova, A. Gargaun, M. V. Berezovski and A. S. Kichkailo, Current and prospective protein biomarkers of lung cancer, *Cancers*, 2017, **9**(11), 155.
3 D. Crosby, S. Bhatia, K. M. Brindle, L. M. Coussens, C. Dive, M. Emberton, S. Esener, R. C. Fitzgerald, S. S. Gambhir and P. Kuhn, Early detection of cancer, *Science*, 2022, **375**(6586), eaay9040.
4 F. Xiang, X. Wang, X. He, Z. Peng, B. Yang, J. Zhang, Q. Zhou, H. Ye, Y. Ma and H. Li, Antibody detection and dynamic characteristics in patients with coronavirus disease 2019, *Clin. Infect. Dis.*, 2020, **71**(8), 1930–1934.
5 J. Zhao, Q. Yuan, H. Wang, W. Liu, X. Liao, Y. Su, X. Wang, J. Yuan, T. Li and J. Li, Antibody responses to SARS-CoV-2 in patients with novel coronavirus disease 2019, *Clin. Infect. Dis.*, 2020, **71**(16), 2027–2034.
6 C. Y.-P. Lee, R. T. Lin, L. Renia and L. F. Ng, Serological approaches for COVID-19: epidemiologic perspective on surveillance and control, *Front. Immunol.*, 2020, **11**, 548159.
7 C. L. Charlton, J. N. Kanji, K. Johal, A. Bailey, S. S. Plitt, C. MacDonald, A. Kunst, E. Buss, L. E. Burnes and K. Fonseca, Evaluation of six commercial mid-to high-volume antibody and six point-of-care lateral flow assays for detection of SARS-CoV-2 antibodies, *J. Clin. Microbiol.*, 2020, **58**(10), e01361.
8 Y. Zhang and H. Noji, Digital bioassays: theory, applications, and perspectives, *Anal. Chem.*, 2017, **89**(1), 92–101.
9 C.-W. Kuo and A. M. Smith, Digital and Absolute Assays for Low Abundance Molecular Biomarkers, *Acc. Chem. Res.*, 2023, **56**(9), 1031–1042.
10 A. S. Basu, Digital assays part II: digital protein and cell assays, *SLAS Technol.*, 2017, **22**(4), 387–405.
11 D. C. Duffy, Digital detection of proteins, *Lab Chip*, 2023, **23**(5), 818–847.
12 D. M. Rissin, C. W. Kan, T. G. Campbell, S. C. Howes, D. R. Fournier, L. Song, T. Piech, P. P. Patel, L. Chang and A. J. Rivnak, Single-molecule enzyme-linked immunosorbent assay detects serum proteins at subfemtomolar concentrations, *Nat. Biotechnol.*, 2010, **28**(6), 595–599.
13 C. W. Kan, C. I. Tobos, D. M. Rissin, A. D. Wiener, R. E. Meyer, D. M. Svancara, A. Comperchio, C. Warwick, R. Millington and N. Collier, Digital enzyme-linked immunosorbent assays with sub-attomolar detection limits based on low numbers of capture beads combined with high efficiency bead analysis, *Lab Chip*, 2020, **20**(12), 2122–2135.
14 K. Leirs, F. Dal Dosso, E. Perez-Ruiz, D. Decrop, R. Cops, J. Huff, M. Hayden, N. Collier, K. X. Yu and S. Brown, Bridging the gap between digital assays and point-of-care testing: automated, low cost, and ultrasensitive detection of thyroid stimulating hormone, *Anal. Chem.*, 2022, **94**(25), 8919–8927.
15 J. Mok, M. N. Mindrinos, R. W. Davis and M. Javanmard, Digital microfluidic assay for protein detection, *Proc. Natl. Acad. Sci. U. S. A.*, 2014, **111**(6), 2110–2115.
16 D. H. Wilson, D. M. Rissin, C. W. Kan, D. R. Fournier, T. Piech, T. G. Campbell, R. E. Meyer, M. W. Fishburn, C. Cabrera and P. P. Patel, The Simoa HD-1 analyzer: a novel fully automated digital immunoassay analyzer with single-molecule sensitivity and multiplexing, *J. Lab. Autom.*, 2016, **21**(4), 533–547.
17 L. Cohen, N. Cui, Y. Cai, P. M. Garden, X. Li, D. A. Weitz and D. R. Walt, Single molecule protein detection with attomolar sensitivity using droplet digital enzyme-linked immunosorbent assay, *ACS Nano*, 2020, **14**(8), 9491–9501.
18 J. Yi, Z. Gao, Q. Guo, Y. Wu, T. Sun, Y. Wang, H. Zhou, H. Gu, J. Zhao and H. Xu, Multiplexed digital ELISA in picoliter droplets based on enzyme signal amplification block and precisely decoding strategy: A universal and practical biodetection platform, *Sens. Actuators, B*, 2022, **369**, 132214.
19 C. Wu, P. M. Garden and D. R. Walt, Ultrasensitive detection of attomolar protein concentrations by dropcast single molecule assays, *J. Am. Chem. Soc.*, 2020, **142**(28), 12314–12323.
20 H. Chen, Z. Li, L. Zhang, P. Sawaya, J. Shi and P. Wang, Quantitation of femtomolar-level protein biomarkers using a simple microbubbling digital assay and bright-field smartphone imaging, *Angew. Chem.*, 2019, **131**(39), 14060–14066.
21 Digital readout platform for water-in-oil droplet immunoassays running on a cell-phone for point of care viral load sensing, *16th International Conference on Miniaturized Systems for Chemistry and Life Sciences, MicroTAS 2012*, ed. P. A. Sandoz, A. F. Coskun, A. J. Chung, W. M. Weaver, O. Adeyiga, D. Khodadadi, A. Ozcan and D.

Open Access Article. Published on 28 July 2025. Downloaded on 11/2/2025 4:17:36 AM.
This article is licensed under a Creative Commons Attribution-NonCommercial 3.0 Unported Licence.

Di Carlo, Chemical and Biological Microsystems Society, 2012.
22 Y. Obayashi, R. Iino and H. Noji, A single-molecule digital enzyme assay using alkaline phosphatase with a cumarin-based fluorogenic substrate, *Analyst*, 2015, **140**(15), 5065–5073.
23 T. Wang, M. Zhang, D. D. Dreher and Y. Zeng, Ultrasensitive microfluidic solid-phase ELISA using an actuatable microwell-patterned PDMS chip, *Lab Chip*, 2013, **13**(21), 4190–4197.
24 K.-H. Su, Q.-H. Wei, X. Zhang, J. Mock, D. R. Smith and S. Schultz, Interparticle coupling effects on plasmon resonances of nanogold particles, *Nano Lett.*, 2003, **3**(8), 1087–1090.
25 E. Prodan, C. Radloff, N. J. Halas and P. Nordlander, A hybridization model for the plasmon response of complex nanostructures, *Science*, 2003, **302**(5644), 419–422.
26 P. K. Jain and M. A. El-Sayed, Plasmonic coupling in noble metal nanostructures, *Chem. Phys. Lett.*, 2010, **487**(4–6), 153–164.
27 P. K. Jain, W. Huang and M. A. El-Sayed, On the universal scaling behavior of the distance decay of plasmon coupling in metal nanoparticle pairs: a plasmon ruler equation, *Nano Lett.*, 2007, **7**(7), 2080–2088.
28 J. J. Storhoff, R. Elghanian, R. C. Mucic, C. A. Mirkin and R. L. Letsinger, One-pot colorimetric differentiation of polynucleotides with single base imperfections using gold nanoparticle probes, *J. Am. Chem. Soc.*, 1998, **120**(9), 1959–1964.
29 R. Elghanian, J. J. Storhoff, R. C. Mucic, R. L. Letsinger and C. A. Mirkin, Selective colorimetric detection of polynucleotides based on the distance-dependent optical properties of gold nanoparticles, *Science*, 1997, **277**(5329), 1078–1081.
30 C. Sönnichsen, B. M. Reinhard, J. Liphardt and A. P. Alivisatos, A molecular ruler based on plasmon coupling of single gold and silver nanoparticles, *Nat. Biotechnol.*, 2005, **23**(6), 741–745.
31 F. Ungureanu, D. Wasserberg, N. Yang, R. Verdoold and R. P. Kooyman, Immunosensing by colorimetric darkfield microscopy of individual gold nanoparticle-conjugates, *Sens. Actuators, B*, 2010, **150**(2), 529–536.
32 R. Verdoold, R. Gill, F. Ungureanu, R. Molenaar and R. P. Kooyman, Femtomolar DNA detection by parallel colorimetric darkfield microscopy of functionalized gold nanoparticles, *Biosens. Bioelectron.*, 2011, **27**(1), 77–81.
33 M. Sriram, B. P. Markhali, P. R. Nicovich, D. T. Bennett, P. J. Reece, D. B. Hibbert, R. D. Tilley, K. Gaus, S. Vivekchand and J. J. Gooding, A rapid readout for many single plasmonic nanoparticles using dark-field microscopy and digital color analysis, *Biosens. Bioelectron.*, 2018, **117**, 530–536.
34 U. Kreibig and M. Vollmer, *Optical Properties of Metal Clusters*, Springer, Berlin, New York, 1995, p. 532.
35 P. K. Jain, K. S. Lee, I. H. El-Sayed and M. A. El-Sayed, Calculated absorption and scattering properties of gold nanoparticles of different size, shape, and composition: applications in biological imaging and biomedicine, *J. Phys. Chem. B*, 2006, **110**(14), 7238–7248, DOI: 10.1021/jp057170o.
36 M. H. Jazayeri, H. Amani, A. A. Pourfatollah, H. Pazoki-Toroudi and B. Sedighimoghaddam, Various methods of gold nanoparticles (GNPs) conjugation to antibodies, *Sens. Biosens. Res.*, 2016, **9**, 17–22.
37 A. Ravindran, P. Chandran and S. S. Khan, Biofunctionalized silver nanoparticles: advances and prospects, *Colloids Surf., B*, 2013, **105**, 342–352.
38 P. Prasher, M. Sharma, H. Mudila, G. Gupta, A. K. Sharma, D. Kumar, H. A. Bakshi, P. Negi, D. N. Kapoor and D. K. Chellappan, Emerging trends in clinical implications of bio-conjugated silver nanoparticles in drug delivery, *Colloid Interface Sci. Commun.*, 2020, **35**, 100244.
39 A. A. Shemetov, I. Nabiev and A. Sukhanova, Molecular interaction of proteins and peptides with nanoparticles, *ACS Nano*, 2012, **6**(6), 4585–4602.
40 S. Rana, Y.-C. Yeh and V. M. Rotello, Engineering the nanoparticle–protein interface: applications and possibilities, *Curr. Opin. Chem. Biol.*, 2010, **14**(6), 828–834.
41 C. D. Spicer, C. Jumeaux, B. Gupta and M. M. Stevens, Peptide and protein nanoparticle conjugates: versatile platforms for biomedical applications, *Chem. Soc. Rev.*, 2018, **47**(10), 3574–3620.
42 D. Bartczak and A. G. Kanaras, Preparation of peptide-functionalized gold nanoparticles using one pot EDC/sulfo-NHS coupling, *Langmuir*, 2011, **27**(16), 10119–10123.
43 R. T. Busch, F. Karim, J. Weis, Y. Sun, C. Zhao and E. S. Vasquez, Optimization and structural stability of gold nanoparticle–antibody bioconjugates, *ACS Omega*, 2019, **4**(12), 15269–15279.
44 M. Retout, H. Valkenier, E. Triffaux, T. Doneux, K. Bartik and G. Bruylants, Rapid and selective detection of proteins by dual trapping using gold nanoparticles functionalized with peptide aptamers, *ACS Sens.*, 2016, **1**(7), 929–933.
45 S. H. Brewer, W. R. Glomm, M. C. Johnson, M. K. Knag and S. Franzen, Probing BSA binding to citrate-coated gold nanoparticles and surfaces, *Langmuir*, 2005, **21**(20), 9303–9307.
46 S. Zhang, Y. Moustafa and Q. Huo, Different interaction modes of biomolecules with citrate-capped gold nanoparticles, *ACS Appl. Mater. Interfaces*, 2014, **6**(23), 21184–21192.
47 V. Banerjee and K. Das, Interaction of silver nanoparticles with proteins: A characteristic protein concentration dependent profile of SPR signal, *Colloids Surf., B*, 2013, **111**, 71–79.
48 J. G. Kenna, G. N. Major and R. S. Williams, Methods for reducing non-specific antibody binding in enzyme-linked immunosorbent assays, *J. Immunol. Methods*, 1985, **85**(2), 409–419, DOI: 10.1016/0022-1759(85)90150-4.
49 M. A. Sentandreu, L. Aubry, F. Toldrá and A. Ouali, Blocking agents for ELISA quantification of compounds coming from bovine muscle crude extracts, *Eur. Food Res. Technol.*, 2007, **224**(5), 623–628, DOI: 10.1007/s00217-006-0348-3.

 © 2025 The Author(s). Published by the Royal Society of Chemistry

Open Access Article. Published on 28 July 2025. Downloaded on 11/2/2025 4:17:36 AM.
This article is licensed under a Creative Commons Attribution-NonCommercial 3.0 Unported Licence.

50 K. Reimhult, K. Petersson and A. Krozer, QCM-D analysis of the performance of blocking agents on gold and polystyrene surfaces, *Langmuir*, 2008, **24**(16), 8695–8700, DOI: 10.1021/la800224s.

51 S. Dominguez-Medina, J. Blankenburg, J. Olson, C. F. Landes and S. Link, Adsorption of a Protein Monolayer via Hydrophobic Interactions Prevents Nanoparticle Aggregation under Harsh Environmental Conditions, *ACS Sustain. Chem. Eng.*, 2013, **1**(7), 833–842, DOI: 10.1021/sc400042h.

52 Z. Tao, Y. Zhou, X. Li and Z. P. Wang, Competitive HRP-Linked Colorimetric Aptasensor for the Detection of Fumonisin B1 in Food based on Dual Biotin-Streptavidin Interaction, *Biosensors*, 2020, **10**(4), 31.

53 Y. L. Jeyachandran, J. A. Mielczarski, E. Mielczarski and B. Rai, Efficiency of blocking of non-specific interaction of different proteins by BSA adsorbed on hydrophobic and hydrophilic surfaces, *J. Colloid Interface Sci.*, 2010, **341**(1), 136–142, DOI: 10.1016/j.jcis.2009.09.007.

54 D. J. Boehmler, Z. J. O'Dell, C. Chung and K. R. Riley, Bovine Serum Albumin Enhances Silver Nanoparticle Dissolution Kinetics in a Size- and Concentration-Dependent Manner, *Langmuir*, 2020, **36**(4), 1053–1061, DOI: 10.1021/acs.langmuir.9b03251.

55 K. M. Fahy, M. K. Eiken, K. V. Baumgartner, K. Q. Leung, S. E. Anderson, E. Berggren, E. Bouzos, L. R. Schmitt, P. Asuri and K. E. Wheeler, Silver Nanoparticle Surface Chemistry Determines Interactions with Human Serum Albumin and Cytotoxic Responses in Human Liver Cells, *ACS Omega*, 2023, **8**(3), 3310–3318, DOI: 10.1021/acsomega.2c06882.

56 M. Dolci, Y. Wang, S. W. Nooteboom, P. E. D. Soto Rodriguez, S. Sanchez, L. Albertazzi and P. Zijlstra, Real-Time Optical Tracking of Protein Corona Formation on Single Nanoparticles in Serum, *ACS Nano*, 2023, **17**(20), 20167–20178, DOI: 10.1021/acsnano.3c05872.

57 J. M. Dennison, J. M. Zupancic, W. Lin, J. H. Dwyer and C. J. Murphy, Protein Adsorption to Charged Gold Nanospheres as a Function of Protein Deformability, *Langmuir*, 2017, **33**(31), 7751–7761, DOI: 10.1021/acs.langmuir.7b01909.

58 A. J. Haes and R. P. Van Duyne, A nanoscale optical biosensor: sensitivity and selectivity of an approach based on the localized surface plasmon resonance spectroscopy of triangular silver nanoparticles, *J. Am. Chem. Soc.*, 2002, **124**(35), 10596–10604, DOI: 10.1021/ja020393x.

59 S. P. Boulos, T. A. Davis, J. A. Yang, S. E. Lohse, A. M. Alkilany, L. A. Holland and C. J. Murphy, Nanoparticle-protein interactions: a thermodynamic and kinetic study of the adsorption of bovine serum albumin to gold nanoparticle surfaces, *Langmuir*, 2013, **29**(48), 14984–14996, DOI: 10.1021/la402920f.

60 A. J. Haes and R. P. Van Duyne, A nanoscale optical biosensor: sensitivity and selectivity of an approach based on the localized surface plasmon resonance spectroscopy of triangular silver nanoparticles, *J. Am. Chem. Soc.*, 2002, **124**(35), 10596–10604.

61 J. Zhao, L. Jensen, J. Sung, S. Zou, G. C. Schatz and R. P. Van Duyne, Interaction of plasmon and molecular resonances for rhodamine 6G adsorbed on silver nanoparticles, *J. Am. Chem. Soc.*, 2007, **129**(24), 7647–7656.

62 M. D. Malinsky, K. L. Kelly, G. C. Schatz and R. P. Van Duyne, Chain length dependence and sensing capabilities of the localized surface plasmon resonance of silver nanoparticles chemically modified with alkanethiol self-assembled monolayers, *J. Am. Chem. Soc.*, 2001, **123**(7), 1471–1482.

63 A. J. Haes, S. Zou, G. C. Schatz and R. P. Van Duyne, Nanoscale optical biosensor: short range distance dependence of the localized surface plasmon resonance of noble metal nanoparticles, *J. Phys. Chem. B*, 2004, **108**(22), 6961–6968.

64 M. Alrahili, Single Silver Nanoparticles: Local Refractive Index Response to Localized Surface Plasmon Resonance and Molar Attenuation Coefficient, *Colloid J.*, 2024, 1–15.

65 S. Busse, V. Scheumann, B. Menges and S. Mittler, Sensitivity studies for specific binding reactions using the biotin/streptavidin system by evanescent optical methods, *Biosens. Bioelectron.*, 2002, **17**(8), 704–710.

66 G. Wenz and P. Liepold, Self-assembly of biotin and thio-functionalized carboxymethyl celluloses on gold and molecular recognition of streptavidin detected by surface plasmon resonance, *Cellulose*, 2007, **14**, 89–98.

67 S. Dominguez-Medina, L. Kisley, L. J. Tauzin, A. Hoggard, B. Shuang, A. S. D. S. Indrasekara, S. Chen, L.-Y. Wang, P. J. Derry and A. Liopo, Adsorption and unfolding of a single protein triggers nanoparticle aggregation, *ACS Nano*, 2016, **10**(2), 2103–2112.

68 R. Cukalevski, S. A. Ferreira, C. J. Dunning, T. Berggård and T. Cedervall, IgG and fibrinogen driven nanoparticle aggregation, *Nano Res.*, 2015, **8**, 2733–2743.

69 L. Wang, J. Li, J. Pan, X. Jiang, Y. Ji, Y. Li, Y. Qu, Y. Zhao, X. Wu and C. Chen, Revealing the binding structure of the protein corona on gold nanorods using synchrotron radiation-based techniques: understanding the reduced damage in cell membranes, *J. Am. Chem. Soc.*, 2013, **135**(46), 17359–17368, DOI: 10.1021/ja406924v.

70 R. X. Huang, R. R. Carney, K. Ikuma, F. Stellacci and B. L. T. Lau, Effects of Surface Compositional and Structural Heterogeneity on Nanoparticle-Protein Interactions: Different Protein Configurations, *ACS Nano*, 2014, **8**(6), 5402–5412, DOI: 10.1021/nn501203k.

71 B. Jachimska, M. Wasilewska and Z. Adamczyk, Characterization of globular protein solutions by dynamic light scattering, electrophoretic mobility, and viscosity measurements, *Langmuir*, 2008, **24**(13), 6866–6872.

72 K. Aslan, C. C. Luhrs and V. H. Pérez-Luna, Controlled and reversible aggregation of biotinylated gold nanoparticles with streptavidin, *J. Phys. Chem. B*, 2004, **108**(40), 15631–15639.

73 M. Retout, I. Jabin and G. Bruylants, Synthesis of Ultrastable and Bioconjugable Ag, Au, and bimetallic Ag_Au nanoparticles coated with calix [4] arenes, *ACS Omega*, 2021, **6**(30), 19675–19684.

Open Access Article. Published on 28 July 2025. Downloaded on 11/2/2025 4:17:36 AM.
This article is licensed under a Creative Commons Attribution-NonCommercial 3.0 Unported Licence.

74 Q. Lenne, M. Retout, B. Gosselin, G. Bruylants, I. Jabin, J. Hamon, C. Lagrost and Y. R. Leroux, Highly stable silver nanohybrid electrocatalysts for the oxygen reduction reaction, *Chem. Commun.*, 2022, **58**(20), 3334–3337.

75 B. Gosselin, M. Retout, R. Dutour, L. Troian-Gautier, R. Bevernaegie, S. Herens, P. Lefèvre, O. Denis, G. Bruylants and I. Jabin, Ultrastable silver nanoparticles for rapid serology detection of anti-SARS-CoV-2 immunoglobulins G, *Anal. Chem.*, 2022, **94**(20), 7383–7390.

76 M. Kincanon and C. J. Murphy, Nanoparticle Size Influences the Self-Assembly of Gold Nanorods Using Flexible Streptavidin–Biotin Linkages, *ACS Nano*, 2023, **17**(23), 24090–24103.

77 A. W. Scott, V. Garimella, C. M. Calabrese and C. A. Mirkin, Universal Biotin–PEG-linked gold nanoparticle probes for the simultaneous detection of nucleic acids and proteins, *Bioconjugate Chem.*, 2017, **28**(1), 203–211.

78 J. Zhao, A. O. Pinchuk, J. M. Mcmahon, S. Z. Li, L. K. Ausman, A. L. Atkinson and G. C. Schatz, Methods for Describing the Electromagnetic Properties of Silver and Gold Nanoparticles, *Acc. Chem. Res.*, 2008, **41**(12), 1710–1720, DOI: **10.1021/ar800028j**.

79 T. Wriedt, Mie theory: a review, *The Mie Theory: Basics and Applications*, 2012, pp. 53–71.

80 V. Myroshnychenko, J. Rodríguez-Fernández, I. Pastoriza-Santos, A. M. Funston, C. Novo, P. Mulvaney, L. M. Liz-Marzán and F. J. G. De Abajo, Modelling the optical response of gold nanoparticles, *Chem. Soc. Rev.*, 2008, **37**(9), 1792–1805.

81 D. D. Evanoff Jr and G. Chumanov, Synthesis and optical properties of silver nanoparticles and arrays, *Chemphyschem*, 2005, **6**(7), 1221–1231, DOI: **10.1002/cphc.200500113**.

82 C. Jing, Z. Gu, Y.-L. Ying, D.-W. Li, L. Zhang and Y.-T. Long, Chrominance to dimension: a real-time method for measuring the size of single gold nanoparticles, *Anal. Chem.*, 2012, **84**(10), 4284–4291.

83 X. Xu, T. Li, Z. Xu, H. Wei, R. Lin, B. Xia, F. Liu and N. Li, Automatic enumeration of gold nanomaterials at the single-particle level, *Anal. Chem.*, 2015, **87**(5), 2576–2581.

84 S. J. Oldenburg, *Light Scattering from Gold Nanoshells*, Rice University, 2000.

 © 2025 The Author(s). Published by the Royal Society of Chemistry